Journal of Materials Chemistry C

ROYAL SOCIETY OF CHEMISTRY

PAPER

View Article Online
View Journal | View Issue

Cite this: J. Mater. Chem. C, 2022, 10, 7674

Formation of magnetic anionic electrons by hole doping

Jingyu He,[a] Yuanzheng Chen,[b] Zishen Wang,[ac] Ming Yang,[d] Tong Yang,[d] Lei Shen,[e] Xiaoguang Xu,[f] Yong Jiang,[f] Jianwei Chai,[g] Lai Mun Wong,[g] Shijie Wang,*[g] Yuan Ping Feng*[ac] and Jun Zhou*[g]

Received 10th February 2022,
Accepted 16th April 2022

DOI: 10.1039/d2tc00564f

rsc.li/materials-c

Electrides intrinsically hold some unique properties arising from the anionic electrons such as the low work function from their loosely bound nature and extended distribution due to their absence of restriction from atomic orbitals. Leveraging these properties, *via* first-principles calculations, we firstly propose a new nonmagnetic semiconducting electrene $ZrCl_2$ ($[ZrCl_2]^{2+}\cdot 2e^-$), which is stable and can be easily exfoliated from its experimentally grown parent layered bulk. Moreover, a spontaneous spin splitting of the anionic electrons and consequently a nonmagnetic–magnetic phase transition are revealed in monolayer $ZrCl_2$ at a critical doping concentration of 5.0×10^{14} cm^{-2}. Assisted by the low-energy effective model, constrained random phase approximation simulation, and Anderson's theory, we demonstrate the mechanism of d^0 magnetism in the doped monolayer $ZrCl_2$ and confirm the dual localized and extended nature of these magnetic anionic electrons. These results enable electric-field controllable magnetism in electrenes, showing potential for novel spintronic applications.

Introduction

The experimental growth of truly two-dimensional (2D) magnets CrI_3 and $CrGeTe_3$ in 2017 has ignited research enthusiasm in the materials community for low-dimensional magnetism.[1,2] Hitherto, this group of materials has burgeoned and a wide spectrum of emergent properties have been reported such as controllable magnetic phase transition by external stimuli and spin-valley coupled excitonic physics, making them appealing for new spintronic and valleytronic applications.[3–6] However, the origin of the magnetic moments of the most reported 2D magnets is akin to the conventional three-dimensional magnetic materials, that is, from the magnetic elements (Fe, Cr, V, and Mn), in which the d orbitals are partially occupied such as in the recently reported FeX_3 (X = F, Cl, Br and I) and Janus VSeTe systems.[7–11]

On the other hand, the so-called d^0 magnetism, which does not involve magnetic elements, has been known for a while.[12–14] To achieve such unconventional magnetism, a shift of the Fermi level (E_F) by carrier doping, defect formation, or functionalities, is usually needed to obtain partially filled p orbitals, which increases the density of states (DOS) at the Fermi level.[15–17] This facilitates a Stoner-type itinerant magnetic instability, which can be triggered by $N(E_F)I > 1$, where $N(E_F)$ is the density of states at the Fermi energy and I represents the Stoner parameter, respectively.[18] However, due to the less localized nature of p orbitals than d orbitals, the Stoner parameters of d^0 systems are usually smaller than that of typical 3d ferromagnets. This suggests that the d^0 magnetic instability is mainly driven by the high $N(E_F)$. As a result, materials with Mexican-hat-induced van Hove singularities with power-law divergent DOS are ideal examples for d^0 magnetism.[19–22]

Recently, an intrinsic d^0 magnetism has been proposed in monolayer electrides (coined as electrenes).[23–25] This is based on electrenes being electron-rich and their excess electrons localizing at the interstitial sites at the center of cation "cages" (called anionic electrons).[26] The localized nature of the anionic electrons leads to a strong correlation (thus a large I) and a narrow bandwidth [thus a high $N(E_F)$], both of which promote the system to meet the Stoner criterion and induce spontaneous splitting of the anionic electrons. Such atomic

[a] Department of Physics, National University of Singapore, Singapore 117551, Singapore. E-mail: phyfyp@nus.edu.sg
[b] School of Physical Science and Technology, Southwest Jiaotong University, Chengdu 610031, China
[c] Center for Advanced Two-Dimensional Materials (CA2DM), National University of Singapore, Singapore 117546, Singapore
[d] Department of Applied Physics, The Hong Kong Polytechnic University, Hung Hom, Kowloon, Hong Kong SAR, China
[e] Department of Mechanical Engineering, National University of Singapore, Singapore 117575, Singapore
[f] School of Materials Science and Engineering, University of Science and Technology Beijing, Beijing, 100083, China
[g] Institute of Materials Research & Engineering, A*STAR (Agency for Science, Technology and Research), 2 Fusionopolis Way, Innovis, Singapore 138634, Singapore. E-mail: sj-wang@imre.a-star.edu.sg, zhou_jun@imre.a-star.edu.sg

orbital-free magnetic anionic electrons represent a novel pathway for d^0 magnetism, which does not require a van Hove singularization in the DOS. Besides, the wavefunctions of magnetic anionic electrons have extended tails and their overlap results in a strong direct ferromagnetic (FM) coupling between them.[23]

To take advantage of both the tunability of carrier doping and the unique dual nature of anionic electrons, it is interesting to explore the possibility of a charge doping induced magnetism in non-magnetic electrenes. The benefit of this concept is threefold. Firstly, the 2D nature of electrenes allows the application of gate voltage for carrier doping.[16,27] Whereas conventional chemical doping in bulk materials suffers from low carrier density, high expenses at damaging the system's transport properties, and technological limitations, the gate-controlled electrostatic doping has been shown to be a useful technique for both electron and hole doping, achieving high carrier densities exceeding 10^{15} cm^{-2} and is reversible and non-destructive as well as allowing the electrical control of magnetism.[28] Secondly, the localized nature of anionic electrons provides a good condition to fulfill the Stoner criterion by shifting the Fermi level. Finally, their loosely bound nature leads to the low work function of electrenes, which would further facilitate the hole doping of electrenes.

To exemplify this concept, *via* first-principles simulations, we first propose a new electrene, *i.e.*, a $ZrCl_2$ monolayer. It is a non-magnetic semiconductor, which can be easily exfoliated from the experimentally grown parent bulk structure and is dynamically and thermodynamically stable. More importantly, our results confirm that its anionic electrons become spin-polarized after a critical hole doping concentration of 5.0×10^{14} cm^{-2}. The induced magnetic anionic electrons also demonstrate a unique dual localized and extended nature, and thus a large magnetic exchange coupling. These results pave the way to generate tunable magnetic electrenes for novel spintronic applications.

Methods

All the density functional theory (DFT) calculations were performed using the Vienna *ab initio* Simulation Package (VASP 6.1.0)[29,30] with the Perdew–Burke–Ernzerhof (PBE) approximation for the exchange–correlation functional and the frozen-core all-electron projector augmented wave (PAW) method for the electron–ion interaction.[31] The plane wave expansion was found to be well converged at a cutoff energy of 450 eV. A Γ-centered $15 \times 15 \times 1$ k-point grid was used to sample the reciprocal space. The structures were fully relaxed until the energy and force were converged to 10^{-6} eV and 0.001 eV $Å^{-1}$, respectively. The thickness of the vacuum layer was set to around 30 Å to eliminate the interaction between the images resulting from the periodic boundary conditions. The Wannier function was constructed from the results of the DFT calculations using the procedure of maximal localization using the Wannier90 package as implemented in VASP.[32] Interstitial-centered maximally-localised Wannier functions (MLWFs) from interstitial s orbitals have been used as initial guesses to construct the MLWFs of the anionic electrons, which were used for further constrained random phase approximation (cRPA) calculations and the long-energy effective model.[33,34]

The Monte Carlo simulations are based on the Heisenberg model and are performed using the VAMPIRE package.[35] The simulated spin system contains 34 800 spins. At each temperature, the orientations of spins were initially randomized, and all the spins were first thermalized for 10, 000 equilibrium steps and then by 50, 000 averaging steps to derive the thermal equilibrium magnetization. The simulated temperature dependent magnetization is fitted to the Curie–Bloch equation in the classical limit $M(T) = (1 - T/T_c)^{\beta}$, where β is the critical exponent.

Results and discussion

The structure of monolayer $ZrCl_2$ is shown in Fig. 1a. It is composed of a middle layer of Zr atoms sandwiched by two Cl atomic layers in trigonal prismatic coordination. This structure resembles an H-phase MoS_2 structure with a space group of $P\bar{6}m2$. It is interesting to note that the layered bulk 3R $ZrCl_2$, containing three H-phase $ZrCl_2$ monolayers in one unit cell, has been experimentally synthesized in the 1970s.[36] However, the experimental report of the monolayer limit of H-phase $ZrCl_2$ is still missing. To explore the synthesizability of monolayer $ZrCl_2$, its exfoliation energy is estimated from the difference of the energy per atom between bulk and monolayer structures and compared to that of graphene and electrene Ca_2N. The exfoliation energy of $ZrCl_2$ (69.0 meV per atom) is much lower than that of electrene 2D Ca_2N (260.0 meV per atom) and comparable to that of graphene (67.0 meV per atom).[37] It is noted that, besides graphene,[38] the electrene Ca_2N has also been experimentally exfoliated, and the anionic electrons in Ca_2N are well retained in the monolayer limit.[39,40] Thus, our results indicate that monolayer $ZrCl_2$ could be exfoliated in the experiment. Besides, the dynamic stability of monolayer $ZrCl_2$ is proved by the phonon band structure (see Fig. 1b) as

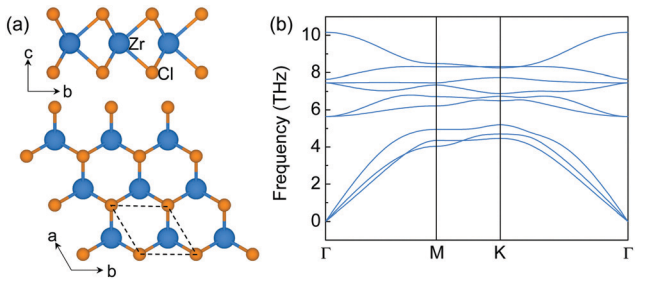

Fig. 1 (a) The top (upper) and side (lower) view of the structure of monolayer $ZrCl_2$ ($[ZrCl_2]^{2+}\cdot 2e^-$) in the H-phase. The dashed lines denote the unit cell, where the blue balls represent the Zr atoms, and the orange ones represent the Cl atoms. (b) The phonon band structure of monolayer $ZrCl_2$.

evidenced by the absence of imaginary frequencies. Its thermodynamical stability is confirmed by the energy above hull,[41] which is 0 eV per atom, indicating its stability against decomposition and phase transition.[42]

The electronic properties of monolayer $ZrCl_2$ are shown in Fig. 2. It is clear that $ZrCl_2$ is a nonmagnetic semiconductor with an indirect PBE gap of 0.94 eV between the valence band maximum at the K point and conduction band minimum along the ΓK path, which are mainly composed of the states from the interstitial sites (denoted as X) and both the Zr d orbitals and X sites, respectively. It is interesting to note that the valence band, which spans from around −1.0 to 0.0 eV, is well separated from other bands. This suggests that the two electrons occupying the isolated valence band have minimal hybridization with other orbitals. In addition, based on the preferred oxidization state of Zr^{4+} and Cl^- ions, $ZrCl_2$ is an intrinsic electron-rich material with 2 excess electrons per formula unit (f.u.), thus it can be written as $[ZrCl_2]^{2+}\cdot 2e^-$. These two facts are typical features of electrides, in which the excess electrons localize at the interstitial site and are loosely bound to the cation framework.

To evince the electride nature of $ZrCl_2$, we performed simulations on the electron localization function (ELF), projected density of states (PDOS), and partial charge for the isolated band. As shown by the ELF in Fig. 2b, a remarkable number of electrons localize at the interstitial centers of the hexagons, performing as anionic electrons (X). To further confirm the existence of interstitial localized electrons in this material, we put a pseudo-atom (an empty sphere) at site X and project DOS on it. As shown by PDOS of $ZrCl_2$ in Fig. 2c, the valence band is contributed mostly by the pseudo-atom X. Such contribution is also evidenced by the real-space distribution of the valence band decomposed charge densities (see Fig. 2d). These results clearly demonstrate that the 2 excess electrons of $ZrCl_2$, which fully occupy the valence band, localize at the interstitial sites as anionic electrons, proving the electride nature of $ZrCl_2$. Thus, we refer to the valence band as an anionic electron band in the following sections.

One of the unique features of electrides is their low work function, because anionic electrons are loosely bound in electrides, and they can easily "escape" from the lattice, making electrides efficient thermionic emitters.[43] The calculated work function of monolayer $ZrCl_2$ is 3.85 eV, which is comparable with that of another electrene Y_2C[44] but lower than those of monolayer transition metal dichalcogenides (TMDs).[45] Recently, a remarkable high doping concentration of $\sim 4 \times 10^{14}$ cm^{-2} has been experimentally applied to 2D semiconductor $CrGeTe_3$.[46] For a direct comparison, the work function of $CrGeTe_3$ is also calculated, which is 4.97 eV, much higher than that of $ZrCl_2$, suggesting the experimental feasibility of heavy doping of $ZrCl_2$. This motivated us to further investigate the doping effects on monolayer $ZrCl_2$.

Hole doping of a series of concentrations up to 10.0×10^{14} cm^{-2} (equivalent to 1 hole per f.u.) with an incremental step of 0.5×10^{14} cm^{-2} has been applied to the monolayer $ZrCl_2$. As shown by the doping concentration-dependent magnetic moments in Fig. 3, a transition from the intrinsic nonmagnetic nature of $ZrCl_2$ to a magnetic state happened at around 5.0×10^{14} cm^{-2}. The magnetic moment of the system further increases with the hole doping concentration and reaches 1 μ_B per f.u. at 10.0×10^{14} cm^{-2} (1 hole per f.u.), implying the full spin polarization of the anionic electron band. Such a hole-induced spin polarization can be understood by the Stoner criterion $N(E_F)I > 1$. As shown in Fig. 2c, the anionic electron band consists of two regions, below and above around −0.5 eV, with high and low DOS, respectively. This is in line with the dual localized and extended nature of anionic electrons as proposed in ref. 18. The hole doping shifts the Fermi level to a lower energy region, which first enters the low DOS zone of −0.5 to 0 eV, where the Stoner criterion is not met due to the small $N(E_F)$. This explains why monolayer $ZrCl_2$ remains nonmagnetic under the doping concentration from 0 to 4.50×10^{14} cm^{-2}. At around 0.5 eV, there is a sudden surge

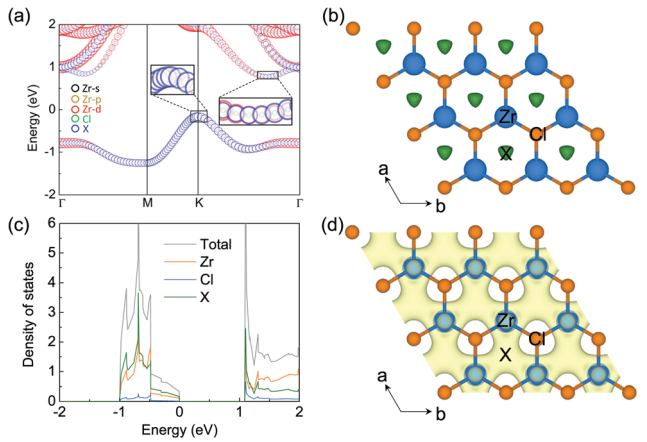

Fig. 2 (a) Band structure and (b) ELF diagram (an isosurface value of 0.6) for monolayer $ZrCl_2$. The green gathering in the hexagonal center is labeled as X. The Zr atoms and Cl atoms are shown in blue and orange, respectively. (c) PDOS of pristine monolayer $ZrCl_2$ with contribution from anionic electrons highlighted by the green line. The Fermi level is shifted to 0 eV in (a) and (c). (d) The decomposed charge density of the isolated band in (a) for the $ZrCl_2$ monolayer (an isosurface value of 1.5×10^{-2} e $Å^{-3}$).

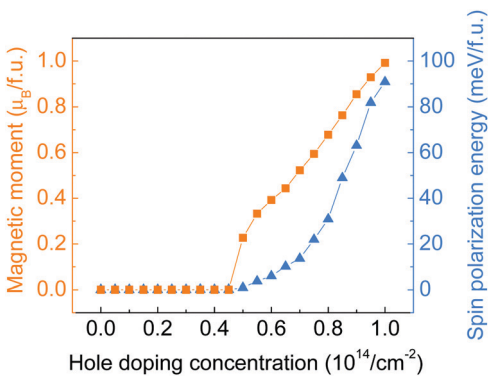

Fig. 3 Total magnetic moment (in orange) and spin polarization energy (in blue) of monolayer $ZrCl_2$ with regards to the hole doping concentration.

of DOS, which leads to the sudden increase of magnetic moments at a doping concentration of around 5.0×10^{14} cm^{-2}.

To study the stability of the magnetic state of the hole-doped $ZrCl_2$, the spin polarization energy, which is defined as the energy difference between the nonmagnetic and ferromagnetic states, is calculated for each doping concentration. Positive values indicate a preference for the ferromagnetic order. As shown by the blue triangles in Fig. 3, the spin polarization energy is positive from the onset of the magnetic state. The spin polarization energy continues to increase with the doping concentration and reaches 90.8 meV per f.u. at 10.0×10^{14} cm^{-2}.

The origin of the magnetic moments in the hole-doped $ZrCl_2$ is further studied by using a hole concentration of 8.0×10^{14} cm^{-2} as an example, under which the total magnetic moment is 0.68 μ_B per f.u. As indicated by the projected density of states shown in Fig. 4a, the magnetic moments come from the spin-splitting of the anionic electron band. And the contribution of the anionic electron site X (green line in Fig. 4a and the inset) is comparable to that of the Zr atom (orange line in Fig. 4a), suggesting the formation of magnetic anionic electrons. The spin density shown in Fig. 4b also confirms that the magnetic moments of the system are mainly from the interstitial sites.

The magnetic anionic electrons have been shown to possess interesting properties such as a dual localized and extended nature.[23] While the localization leads to the formation of magnetic moments, the overlap of the extended tails of the anionic electron wave function produces a strong long-distance direct FM coupling.[23] Unfortunately, such characteristics of the anionic electron cannot be fully captured by conventional DFT. To confirm such properties of the magnetic anionic electrons in hole-doped monolayer $ZrCl_2$, a low-energy effective model is adopted for the anionic electron bands under the hole doping concentration of 8.0×10^{14} cm^{-2}, the Hamiltonian of which based on the second quantization is given as follows.[33,34]

$$\tilde{H} = \sum_{ij,\sigma\sigma'} t_{ij}^{\sigma\sigma'} \hat{c}_{i\sigma}^{\dagger} \hat{c}_{j\sigma'} + \frac{1}{2} \sum_{i,\sigma\sigma'} U_{ii} \hat{c}_{i\sigma}^{\dagger} \hat{c}_{i\sigma'}^{\dagger} \hat{c}_{i\sigma'} \hat{c}_{i\sigma} + \frac{1}{2} \sum_{ij,\sigma\sigma'} U_{ij} \hat{c}_{i\sigma}^{\dagger} \hat{c}_{j\sigma'}^{\dagger} \hat{c}_{j\sigma'} \hat{c}_{i\sigma} + \frac{1}{2} \sum_{ij,\sigma\sigma'} J_{ij}^{D} \hat{c}_{i\sigma}^{\dagger} \hat{c}_{j\sigma'}^{\dagger} \hat{c}_{i\sigma'} \hat{c}_{j\sigma} \quad (1)$$

where $i(j)$, σ (σ'), $\hat{c}_i\left(\hat{c}_i^{\dagger}\right)$, t_{ij}, U_{ii}, U_{ij} and J_{ij}^{D} are site indices, spin indices, creation (annihilation) operators, hopping parameters, on-site Coulomb, off-site Coulomb, and off-site direct-exchange interactions, respectively. The magnitude of Coulomb and exchange interactions can be mapped by the constrained random phase approximation based on the interstitial-centered MLWFs for the anionic electrons. In this work, we focus on the interactions between the nearest neighbouring magnetic anionic electrons.

The calculated parameters are U_{00} = 1.99 eV, U_{01} = 1.34 eV, t_{01} = 76.80 meV and J_{01}^{D} = 31.86 meV. Compared with the anionic electrons in the H-phase $LaBr_2$, the on-site Coulomb interaction is smaller while the off-site direct-exchange interactions and hopping integrals are larger for hole-doped $ZrCl_2$.[23] This suggests that the anionic electrons in $ZrCl_2$ are more delocalized, as supported by its larger bandwidth ($\sim$1.0 eV) than that of H-phase $LaBr_2$ ($\sim$0.5 eV). Nevertheless, the Coulomb interactions and hopping integrals of hole-doped $ZrCl_2$ still satisfy the condition $U_{00} > U_{01} \gg t_{01}$, which facilitates the application of Anderson's model. As a result, the overall isotropic exchange interactions of the hole-doped $ZrCl_2$ monolayer can be determined as follows.[47]

$$J_{01} = \frac{2t_{01}}{\tilde{U}_{01}} - J_{01}^{D} \quad (2)$$

where $\tilde{U}_{01} = U_{00} - U_{01}$ is the effective Coulomb interaction. The first term arises from the antiferromagnetic (AFM) kinetic superexchange from direct hopping between magnetic anionic electrons and the second term is the ferromagnetic (FM) direct exchange from the overlap of the wave functions of magnetic anionic electrons. Using the obtained parameters, we conclude that the isotropic magnetic exchange between the anionic electrons is 28.04 meV, which is larger than that of H-phase $LaBr_2$ and comparable to that of the 2D magnetic materials with high Curie temperature.[48] Importantly, the hole-doped monolayer $ZrCl_2$ is a 2D magnet with an out-of-plane easy axis ($E[100] - E[001]$ = 0.98 meV per formula unit). And our Monte Carlo simulations predict its Curie temperature to be 343 K [see Fig. 4(d)].

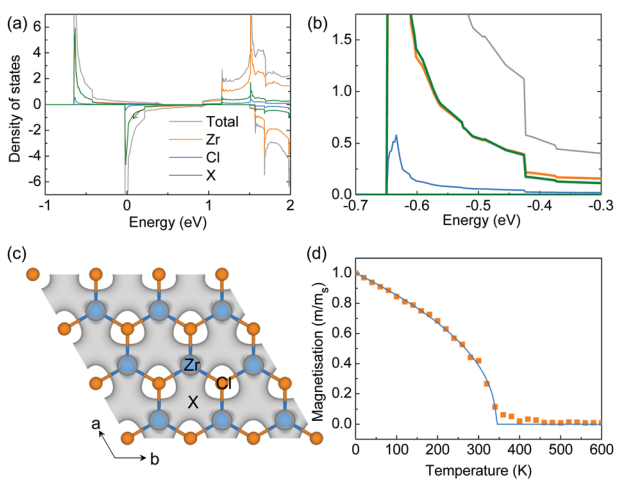

Fig. 4 (a) PDOS of monolayer $ZrCl_2$ under a hole doping concentration of 8.0×10^{14} cm^{-2}. (b) The zoom-in view of PDOS. The contribution of the empty sphere is represented by the green line and that of Zr atoms by the orange line. The Fermi level is shifted to 0 eV. (c) Spin density (grey cloud) for the hole-doped monolayer $ZrCl_2$, where X labels the center site of the hexagon (an isosurface value of 3.0×10^{-3} e Å^{-3}). (d) Temperature-dependent normalized magnetization of the hole-doped monolayer $ZrCl_2$.

Conclusions

In summary, we identify a new nonmagnetic semiconducting electrene $[ZrCl_2]^{2+}\cdot 2e^-$, which is both kinetically and thermodynamically stable and can be exfoliated from the experimentally grown

layered bulk. Taking advantage of the low work function of electrene, our research further shows that at a critical hole doping concentration of 5.0×10^{14} cm^{-2}, the anionic electrons in monolayer $ZrCl_2$ undergo spontaneous spin splitting. Our combined low-energy effective model, cRPA simulation, and Anderson's model confirm the dual localized and extended nature of the hole-induced magnetic anionic electrons in $ZrCl_2$ and their strong ferromagnetic exchange coupling. Our results utilize the intrinsic properties of electrenes to introduce low-dimensional magnetism to non-magnetic systems, paving the way for controllable novel spintronic applications.

Author contributions

Z. J., S. J. W. and Y. P. F. conceived the idea. J. H. performed the DFT calculations with input from Z. J., S. J. W. and Y. P. F. All authors analysed the data. Z. J. and J. H. wrote the manuscript. All authors discussed the results and commented on the manuscript.

Conflicts of interest

There are no conflicts to declare.

Acknowledgements

This work was supported by the Ministry of Education, Singapore, under its MOE Tier 1 Awards R-144-000-441-114 & R-144-000-413-114. We acknowledge the computational resources supported by the National Supercomputing Centre (NSCC) Singapore and Centre of Advanced 2D Materials (CA2DM) HPC infrastructure.

References

1 C. Gong, L. Li, Z. Li, H. Ji, A. Stern, Y. Xia, T. Cao, W. Bao, C. Wang, Y. Wang, Z. Q. Qiu, R. J. Cava, S. G. Louie, J. Xia and X. Zhang, *Nature*, 2017, **546**, 265–269.
2 B. Huang, G. Clark, E. Navarro-Moratalla, D. R. Klein, R. Cheng, K. L. Seyler, D. Zhong, E. Schmidgall, M. A. McGuire, D. H. Cobden, W. Yao, D. Xiao, P. Jarillo-Herrero and X. Xu, *Nature*, 2017, **546**, 270–273.
3 C. Gong and X. Zhang, *Science*, 2019, **363**, 706.
4 B. Huang, M. A. McGuire, A. F. May, D. Xiao, P. Jarillo-Herrero and X. Xu, *Nat. Mater.*, 2020, **19**, 1276–1289.
5 M. Gibertini, M. Koperski, A. F. Morpurgo and K. S. Novoselov, *Nat. Nanotechnol.*, 2019, **14**, 408–419.
6 K. S. Burch, D. Mandrus and J. G. Park, *Nature*, 2018, **563**, 47–52.
7 Z. Guan, J. Wang, J. Huang, X. Wu, Q. Li and J. Yang, *J. Phys. Chem. C*, 2014, **118**, 22491–22498.
8 M. Zhang, Z. Guan, Z. Yang, X. Hu, X. Wang, Y.-Z. Long and C. Huang, *Chem. Mater.*, 2020, **32**, 9001–9007.
9 Z. Guan and S. Ni, *Nanoscale*, 2020, **12**, 22735–22742.
10 Z. Guan and S. Ni, *ACS Appl. Mater. Interfaces*, 2020, **12**, 53067–53075.
11 Z. Guan and S. Ni, *ACS Appl. Electron. Mater.*, 2021, **3**, 3147–3157.
12 J. M. D. Coey, *Nat. Mater.*, 2019, **18**, 652–656.
13 H. Peng, H. J. Xiang, S. H. Wei, S. S. Li, J. B. Xia and J. Li, *Phys. Rev. Lett.*, 2009, **102**, 017201.
14 J. M. D. Coey, *Solid State Sci.*, 2005, **7**, 660–667.
15 R. R. Nair, M. Sepioni, I. L. Tsai, O. Lehtinen, J. Keinonen, A. V. Krasheninnikov, T. Thomson, A. K. Geim and I. V. Grigorieva, *Nat. Phys.*, 2012, **8**, 199–202.
16 M. M. Ugeda, I. Brihuega, F. Guinea and J. M. Gomez-Rodriguez, *Phys. Rev. Lett.*, 2010, **104**, 096804.
17 J. Zhou, Q. Wang, Q. Sun, X. S. Chen, Y. Kawazoe and P. Jena, *Nano Lett.*, 2009, **9**, 3867–3870.
18 E. C. Stoner, *Proc. R. Soc. London, Ser. A*, 1938, **165**, 372–414.
19 T. Cao, Z. Li and S. G. Louie, *Phys. Rev. Lett.*, 2015, **114**, 236602.
20 L. Seixas, A. S. Rodin, A. Carvalho and A. H. Castro Neto, *Phys. Rev. Lett.*, 2016, **116**, 206803.
21 Y. Wang, Q. Zhang, Q. Shen, Y. Cheng, U. Schwingenschlögl and W. Huang, *J. Mater. Chem. C*, 2017, **5**, 4520–4525.
22 L. Guan and J. Tao, *Phys. Rev. Appl.*, 2017, **8**, 064019.
23 J. Zhou, Y. P. Feng and L. Shen, *Phys. Rev. B*, 2020, **102**, 180407(R).
24 J. Zhou, X. Song, M. Yang, J. Chai, N. L. M. Wong, L. Shen, S. Wang and Y. P. Feng, *J. Mater. Chem. C*, 2021, **9**, 16576–16580.
25 X. Sui, J. Wang, C. Yam and B. Huang, *Nano Lett.*, 2021, **21**, 3813–3819.
26 J. L. Dye, *Science*, 2003, **301**, 607–608.
27 S. Jiang, L. Li, Z. Wang, K. F. Mak and J. Shan, *Nat. Nanotechnol.*, 2018, **13**, 549–553.
28 A. M. Goldman, *Annu. Rev. Mater. Res.*, 2014, **44**, 45–63.
29 G. Kresse and J. Hafner, *Phys. Rev. B: Condens. Matter Mater. Phys.*, 1993, **47**, 558–561.
30 G. Kresse and J. Hafner, *Phys. Rev. B: Condens. Matter Mater. Phys.*, 1994, **49**, 14251–14269.
31 G. Kresse and D. Joubert, *Phys. Rev. B: Condens. Matter Mater. Phys.*, 1999, **59**, 1758–1775.
32 A. A. Mostofi, J. R. Yates, Y.-S. Lee, I. Souza, D. Vanderbilt and N. Marzari, *Comput. Phys. Commun.*, 2008, **178**, 685–699.
33 V. V. Mazurenko, A. N. Rudenko, S. A. Nikolaev, D. S. Medvedeva, A. I. Lichtenstein and M. I. Katsnelson, *Phys. Rev. B*, 2016, **94**, 214411.
34 I. V. Solovyev, Z. V. Pchelkina and V. V. Mazurenko, *CrystEngComm*, 2014, **16**, 522–531.
35 R. F. Evans, W. J. Fan, P. Chureemart, T. A. Ostler, M. O. Ellis and R. W. Chantrell, *J. Phys.: Condens. Matter*, 2014, **26**, 103202.
36 A. Cisar, J. D. Corbett and R. L. Daake, *Inorg. Chem.*, 1979, **18**, 836–843.
37 J. Zhou, L. Shen, M. D. Costa, K. A. Persson, S. P. Ong, P. Huck, Y. Lu, X. Ma, Y. Chen, H. Tang and Y. P. Feng, *Sci. Data*, 2019, **6**, 86.
38 K. S. Novoselov, A. K. Geim, S. V. Morozov, D. Jiang, Y. Zhang, S. V. Dubonos, I. V. Grigorieva and A. A. Firsov, *Science*, 2004, **306**, 666–669.

39 D. L. Druffel, K. L. Kuntz, A. H. Woomer, F. M. Alcorn, J. Hu, C. L. Donley and S. C. Warren, *J. Am. Chem. Soc.*, 2016, **138**, 16089–16094.
40 J. S. Oh, C. J. Kang, Y. J. Kim, S. Sinn, M. Han, Y. J. Chang, B. G. Park, S. W. Kim, B. I. Min, H. D. Kim and T. W. Noh, *J. Am. Chem. Soc.*, 2016, **138**, 2496–2499.
41 A. Jain, S. P. Ong, G. Hautier, W. Chen, W. D. Richards, S. Dacek, S. Cholia, D. Gunter, D. Skinner, G. Ceder and K. A. Persson, *APL Mater.*, 2013, **1**, 011002.
42 G. Hautier, A. Jain, S. P. Ong, B. Kang, C. Moore, R. Doe and G. Ceder, *Chem. Mater.*, 2011, **23**, 3495–3508.
43 Y. Toda, S. W. Kim, K. Hayashi, M. Hirano, T. Kamiya, H. Hosono, T. Haraguchi and H. Yasuda, *Appl. Phys. Lett.*, 2005, **87**, 254103.
44 W. Meng, X. Zhang, Y. Liu, X. Dai, H. Gao and G. Liu, *J. Mater. Chem. C*, 2021, **9**, 15477–15487.
45 C. Gong, H. Zhang, W. Wang, L. Colombo, R. M. Wallace and K. Cho, *Appl. Phys. Lett.*, 2013, **103**, 053513.
46 I. A. Verzhbitskiy, H. Kurebayashi, H. Cheng, J. Zhou, S. Khan, Y. P. Feng and G. Eda, *Nat. Electron.*, 2020, **3**, 460–465.
47 P. W. Anderson, *Phys. Rev.*, 1959, **115**, 2–13.
48 A. Kabiraj, M. Kumar and S. Mahapatra, *npj Comput. Mater.*, 2020, **6**, 35.